JACS
JOURNAL OF THE AMERICAN CHEMICAL SOCIETY

ARTICLE

pubs.acs.org/JACS

Magnetite Colloidal Nanocrystals: A Facile Pathway To Prepare Mesoporous Hematite Thin Films for Photoelectrochemical Water Splitting

Ricardo H. Gonçalves,*,† Bruno H. R. Lima,‡ and Edson R. Leite*,†

Departments of †Chemistry and ‡Materials Engineering, Federal University of Sao Carlos, 13565-905 Sao Carlos, SP, Brazil

Supporting Information

ABSTRACT: In this study, we demonstrate an alternative and promising way to produce hematite photoanodes with high performance and without the addition of doping or catalytic coating. In this approach, we processed hematite thin films using a colloidal dispersion of magnetite nanocrystals as the precursor. The photoelectrochemical characterization shows that the colloidal approach used to process an undoped hematite photoanode produced a high-performance electrode for water photooxidation with an onset potential as low as 0.8 V_{RHE}. This value is comparable to the best results reported in the literature for a hematite photoanode modified with catalytic materials. We demonstrate that pure hematite thin films reach 1.1 mA·cm^{-2} at 1.23 V_{RHE} with back-side illumination.

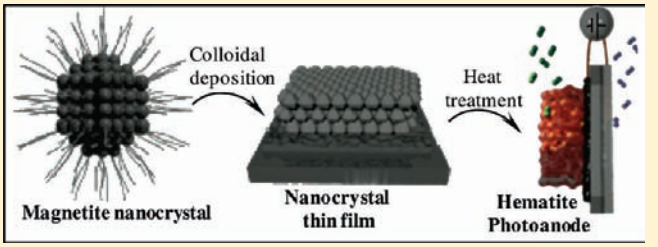

INTRODUCTION

The photoelectrochemical conversion of photon energy into chemical fuel is an alternative approach to storing solar energy. However, many fundamental chemical and materials science challenges must be surmounted to transform this process into a safe and durable procedure.

Hematite (α-Fe_2O_3) has been studied for decades as n-type semiconductor electrode for photoelectrical water splitting. This compound is advantageous in promoting water oxidation due to chemical stability in aqueous alkaline solutions, substantial amounts of visible light absorption, and low cost.[1−3] This semiconductor oxide has a theoretical maximum efficiency of 12.9%;[4] however, the best reported water splitting for doped hematite is 2.1%.[5] Nevertheless, studies have shown that pure hematite performs poorly due to charge recombination and interfacial problems in the hematite/transparent conductor oxide (TCO) solid−solid junction.[6] Two approaches have been used to decrease the charge recombination: (1) modifying the electronic conductivity by doping the hematite with a transition metal and (2) promoting the growth of textured films with the (001) plane oriented vertically to the substrate. It is well known that the conductivity in the basal plane (001) of the hematite is up to 4 orders of magnitude higher than the orthogonal plane.[7] Both approaches should facilitate the collection of electrons during the photooxidation process. The solid−solid junction has been improved by using an intermediate coating between the hematite and the conductor oxide or by adjusting the annealing treatment.[5,8,9]

Many scientists have focused their research on the hematite photoanode to produce oxygen with a reduced anodic overpotential and to improve the overall solar-to-hydrogen conversion efficiencies. In general, these researchers have achieved significant breakthroughs in decreasing the overpotential, and modifying the photoanode surface with the addition of precious metals such as iridium,[10] platinum,[11] ruthenium,[12] or cobalt.[13−16] These chemical elements increase the oxygen kinetic evolution that captures the hole currents on the semiconductor liquid junction.[10] Despite the excellent results and advances reported with the addition of these chemical elements, in our opinion, the pure hematite photoanode could be investigated more thoroughly to improve the anodic overpotential and photocurrent problems by modifying the electrode preparation. We believe that high efficiency depends strongly on the nanostructure,[3] grain boundaries,[8] reduction of lattice defects, and crystallographic orientation. In this case, these structural challenges could be overcome using suitable preparation methods and experimental parameters. Among several methodologies listed in the literature to produce hematite photoanodes, colloidal dispersion deposition has shown promising results.[9] This approach demands an analysis of important variable, before the deposition and heat treatment processes; for example, the surface chemical composition of the inorganic particle, the amount of organic material in the colloidal dispersion, the crystallinity, and the morphology of the nanoparticles. These features have strong influences on the formation of pure hematite that consequently affects the performance of water splitting.

In this study, we demonstrate an alternative and promising way to produce hematite photoanodes with high performance and without the addition of doping or catalytic coating. In this approach, we processed hematite thin films using a colloidal

Received: January 6, 2011
Published: March 28, 2011

Scheme 1. Proposed Pathway to Produce Hematite Thin-Film

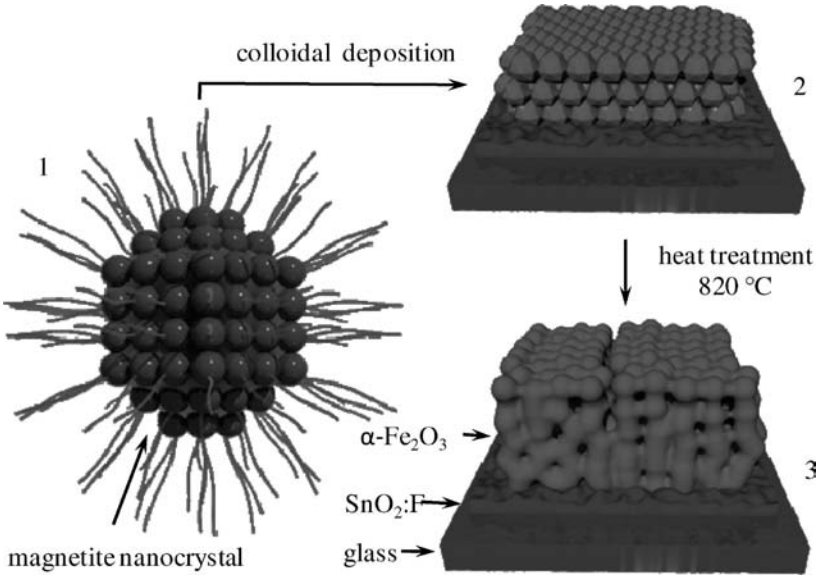

dispersion of magnetite nanocrystals as the precursor. In this method, these nanocrystals were synthesized by a nonaqueous method. This colloidal synthesis was carried out using oleyl alcohol as the solvent and iron(III) acetylacetonate as the precursor. The solution was heated to complete the thermal decomposition of the organometallic compound under an argon atmosphere. The magnetite nanocrystals showed a high colloidal stability in an apolar solvent such as chloroform which is a consequence of the chemical bonding of oleyl alcohol at the nanocrystal surface,[17] allowing the deposition of the magnetite nanocrystals on the TCO substrate (SnO_2:F on aluminiumborosilicate glass) and then obtaining a hematite photoanode by annealing at a high temperature.

Recently, researchers reported that the combination of multilayer deposition (where each layer is very thin) and a high sintering temperature favors the development of metal oxide thin films with a columnar grain structure.[18] Actually, we combined the multistep deposition procedure with the oxidation of magnetite nanocrystals at a high sintering temperature, to process the hematite photoanode (see Scheme 1). The first step in this approach consists of the preparation of a very stable colloidal dispersion of magnetite nanocrystals with an organic surface layer in a suitable solvent. This stable colloidal suspension facilitates the deposition of a very thin layer of magnetite which forms a homogeneous and continuous film on the TCO substrate (second step). In the third and final step, this magnetite layer is transformed into a hematite mesoporous film through a suitable combination of multistep deposition and sintering under an oxygen atmospheric flow.

EXPERIMENTAL SECTION

Meterials. Iron(III) acetylacetonate (99,99%), oleyl alcohol, and sodium hydroxide (99,99%) were purchased from Aldrich Chemical Co. The acetone and chloroform were purchased from Tedia Company, Inc. The SnO_2:F on the aluminomborosilicate glass (Solaronix) was used as a TCO substrate.

Synthesis of Magnetite Nanocrystals. Three millimoles of the iron(III) acetylacetonate was dissolved in 35 mL of oleyl alcohol. After complete dissolution, this red solution was heated at 260 °C for 1 h with vigorous stirring under an argon atmosphere. The formed colloidal dispersion was cooled to room temperature and then added to 50 mL of acetone to provoke nanocrystal flocculation. The flocculated magnetite was separated via centrifugation (10 000 rpm for 5 min) and washed three times with high pure ethanol. The black powder obtained ware dispersed in 10 mL of chloroform, forming a stable colloidal dispersion. The solid concentration of the magnetite nanocrystal colloidal dispersion was adjusted to 2.5 $mg \cdot mL^{-1}$ in chloroform.

Preparation of Hematite Photoanode. Prior to the deposition, the TCO substrate was washed with a HCl/HNO_3 solution for 30 min and rinsed several times with pure water. Then, the same substrate was immersed in a sodium hydroxide solution for 30 min and again rinsed with pure water; the substrate was dried at 110 °C for 2 h. The TCO substrate was covered with a circular mask (0.19 cm^2); 10 μL of the magnetite colloid was dripped onto the circular mask and dried for 3 min. The magnetite thin-film was introduced into the tube furnace at 820 °C for 20 min. The thickness was increased layer by layer with an additional 10 μL of magnetite colloid which formed on the hematite and was again introduced into the tube furnace for 20 min per layer at the same sintering temperature. The sintering was performed with an oxygen atmosphere flow.

Characterization. The film morphology and thickness (by cross-sectional analysis of the cleaved sample) were characterized by FE-SEM (Zeiss Supra 35). The crystalline phases were identified by XRD (Rigaku D-Max 200 using Cu Kα radiation). For HRTEM and STEM/EDX analysis, a TECNAI F20 FEI microscopy was used, operating at 200 kV. The HRTEM/STEM and EDX analyses of hematite were obtained from a thin film piece removed from the substrate with a scalpel blade. The powder removed was dispersed in ethanol and dripped on a carbon coated copper grid. The UV−vis absorption spectra were obtained using a Cary 5E UV−vis spectrophotometer.

The XPS measurements were taken in a VG Kratos XSAM HS spectrometer with a base vacuum of 3×10^{-10} mbar, a 250 mm semihemispherical analyzer with nine channeltrons, and a double Mg/Al anode with an energy of 1253.6 eV and 65 W power. Binding energy corrections were made to raw spectra using the handbook reference of Fe $2p_{3/2}$.

The photoelectrochemical measurements were carried out in a standard three-electrode cell using the hematite film as the working

dx.doi.org/10.1021/ja111454f | J. Am. Chem. Soc. 2011, 133, 6012–6019

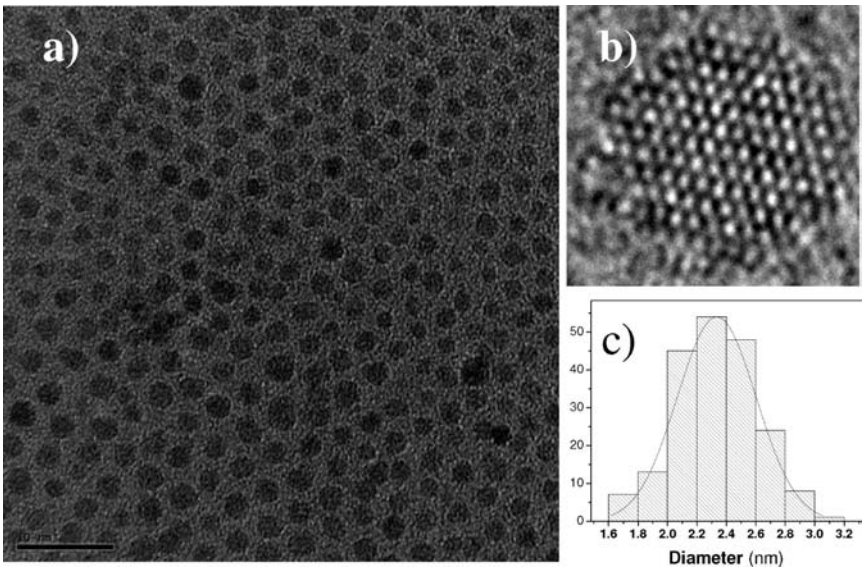

Figure 1. TEM image: (a) low magnification; (b) high resolution of magnetite nanocrystals; (c) size distribution of nanocrystals.

electrode (0.19 cm^2) (Ag/AgCl in a KCl saturated solution as reference electrode and platinum wire as a counter electrode). A 1.0 M NaOH (Merck pro-analysis in high pure water, pH = 13.6, 25 °C) solution was used as the electrolyte. A scanning potentiostat (Potentiostat/Galvanostat μAutolab III) was used to measure the dark and illumination currents at a scan rate of 50 mV/s. Sunlight (1000 W/m^2) was simulated with a 450 W xenon lamp (Osram, ozone free) and AM1.5 filter. The light intensity was set at 100 mW/cm^2. The incident phototo-current conversion efficiency (IPCE) was measured as a function of the excitation wavelength (λ) using a 300 Xe lamp coupled to a Jobin-Ivon monochromator (typical light intensity of 940 $\mu W/cm^2$ at 500 nm). The IPCE was calculated by considering the following eq 1:[5]

$$\text{IPCE} = I(\lambda)1240/E(\lambda)\lambda \quad (1)$$

where $I(\lambda)$ is the photocurrent density ($\mu A \cdot cm^{-2}$), and $E(\lambda)$ is irradiance ($\mu W \cdot cm^{-2}$).

The Mott−Schottky analysis was obtained by an electrochemical impedance spectroscopy (EIS) measurement using an autolab PGSTAT302N with a three-electrode configuration in 1 M of NaOH solution. Frequencies ranging from 100 kHz to 1 Hz, 10 mV of amplitude potential, and a bias voltage of 0.8−1.8 V versus RHE were applied. The EIS was performed in the absence of light, and the Nyquist plot was used to simulate the equivalent circuit to obtain the semiconductor space charge layer capacitance.

RESULTS AND DISCUSSION

The magnetite nanocrystals used as a precursor were first characterized by X-ray powder diffraction (XRD). Figure S1 in Supporting Information shows the formation of magnetite (Fe_3O_4) without an additional phase and a crystallite size of 3.5 nm as calculated by the Scherer equation. The transmission electron microscopy (TEM) image (Figure 1) shows that the size and shape were controlled in this synthetic method, and agglomeration was not observed. The mean nanoparticle size was 2.4 ± 0.2 nm. High-resolution transmission electron microscopy (HRTEM) analysis reveals the single crystal nature of magnetite nanoparticles (Figure 1b).

An important aspect of our approach is the complete transformation of magnetite into hematite during the sintering process. The Fe_3O_4 transforms to gamma-maghemite γ-Fe_2O_3 at 200 °C and γ-Fe_2O_3 is transformed to α-Fe_2O_3 at 450 °C. This last reaction is critical because pure hematite with a minimum amount of defects is obtained just above the Neel point (725 °C).[19] Thus, a sintering temperature that assures the complete elimination of the organic layer and oxidation of magnetite must be selected. However, this temperature cannot promote extensive grain growth and substrate damage. Therefore, rapid thermal annealing was used as a standard sintering procedure. Under optimized experimental conditions, the magnetite nanocrystal was deposited on a TCO substrate and quickly introduced into the tube furnace at 820 °C with an oxygen flow and a soak time of 20 min. The thickness of the hematite thin film has relevant influence on the photoresponse.[20,21] In this case, the hematite thickness was controlled by a dilute colloidal dispersion multideposition step.

The colloidal approach used in this work produced orange-red transparent films with different thicknesses (110, 250, 350, and 930 nm). Figure 2 illustrates the cross-sectional and top-view analyses of the thicker film morphology (processed with six layers) which is characterized by field emission scanning electron microscopy (FE-SEM). The top-view analysis (Figure 2a) exhibits the nanostructured nature of the film with elongated grains (typical size of 50 nm) and open porosity, which characterizes a mesoporous film. The cross-sectional analysis (Figure 2b) shows a film with a thickness of 930 nm and a typical columnar grain structure. Also, a good interface between the TCO and hematite film is apparent as well as the presence of an elongated porous which promote the connection between the top of the hematite film and the TCO surface. An XRD pattern of the thicker film (see Figure 2c) exhibits the formation of a hematite phase with preferential orientation in the [110] axis vertical to the substrate. The thinner films (see Figure S2 in the Supporting Information) show similar cross-sectional and top-view morphologies. A similar XRD pattern was observed for the thinner films. The crystallite size for the thicker film is calculated from XRD data and Scherrer's equation and considers the (110) plane was 36 nm which supports the FE-SEM top-view analysis.

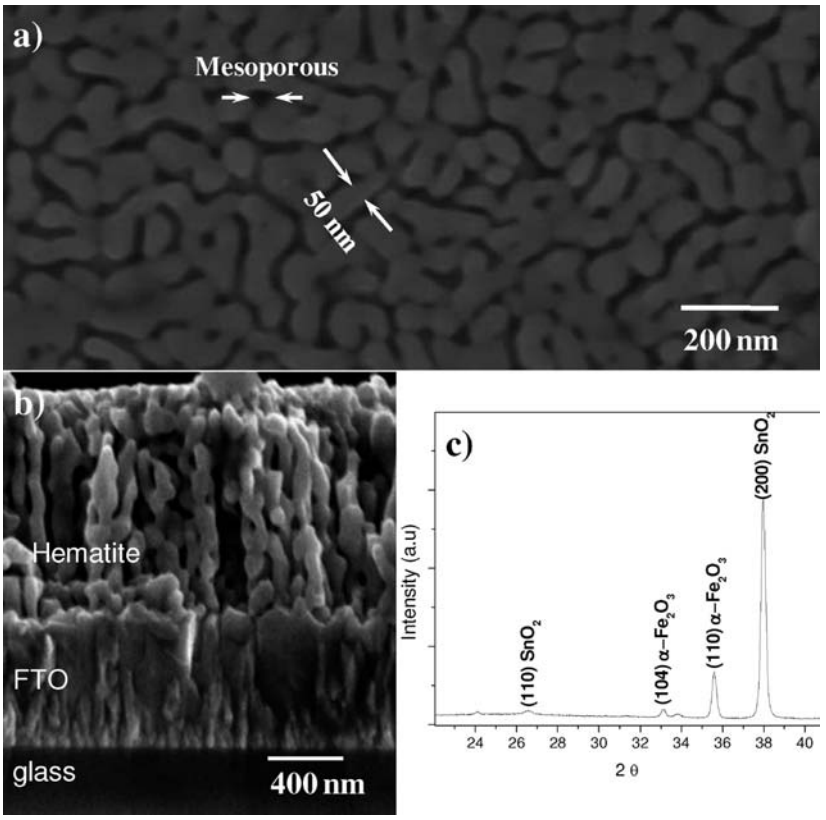

Figure 2. In-lens detector secondary electron images of a film with six layers; (a) top view of an FE-SEM image of the same thin film; (b) FE-SEM image of a hematite thin film on the TCO substrate (cross section); (c) XRD pattern of the film formed by six layers.

The film was also characterized by HRTEM and scanning transmission electron microscopy (STEM). Figure 3a shows a high magnification HRTEM image of a piece of hematite film removed from the substrate. In this image, two grains (apparently in two different zone axes) are apparent. However, a refined analysis of the HRTEM image reveals that these grains are positioned in a different focus position (in a different height). When the fast Fourier transform (FFT) pattern was calculated at different points of the image, the same FFT pattern was obtained. The sum of two distinct regions of the FFT pattern reveals that the hematite grains are oriented along the [110] zone axis (see Figure 3b) which confirms the preferential orientation observed by XRD analysis. Different elongated grains were also analyzed which frequently revealed the orientation of these grains along the [001] zone axis (see Figure 3c). These results strongly support the growth of columnar grains of hematite with an (001) plane oriented vertically to the substrate. The STEM analysis was performed to obtain chemical information about the hematite film by energy-dispersive X-ray analysis (EDX). The EDX analysis did not show the presence of tin (Sn) or other chemical contaminants (see Figure S3 in Supporting Information), indicating that even at high sintering temperatures no interdiffusion process takes place. This analysis was performed with a high exposure time which assured a good signal-to-noise ratio and reliable results. To support the EDX characterization, an XPS analysis of the hematite photoanode was performed. Because of the low lateral resolution of the XPS analysis (in the present study, illumination is by an X-ray of $\sim$1 cm^2), the direct analysis of the supported film on FTO or even the analysis of a piece of the hematite film removed from the substrate can generate uncertainty about the Sn location. Thus, the hematite film was dissolved (in a 0.1 M water solution of HCl) with subsequent deposition of this solution over a platinum substrate, followed by evaporation of the solution. This procedure facilitated the formation of a $FeCl_3$ film over the platinum substrate. This film was analyzed by XPS (see Figure S4 in the Supporting Information), and no trace of Sn was detected, even for a high exposure analysis time which supports the EDX analysis, indicating that the Sn concentration is below the detection level of both analyses (below $\sim$1000 ppm).

The microstructural characterization described above shows the growth of a mesoporous hematite thin film with a columnar grain structure which is textured in the [110] zone axis. The crystallite and grain size after the sintering process indicate an intense grain growth process, and the XRD analysis indicates the complete oxidation of magnetite to hematite without unintentional doping by tin or other chemical elements. The mechanism that promoted the textured thin film with a columnar morphology is unknown; however, it must be related to a grain growth process based on a rotational alignment between particles (followed by coalescence).[22]

The optical properties of the hematite photoanode films were characterized by UV−vis spectroscopy. Figure 4 shows the absorbance spectrum of the films with different thicknesses. The absorption onset between 550 and 600 nm for all samples is consistent with a 2.1−2.2 eV band gap of the hematite reported by several researchers.[23,24] Typical electronic transitions reported for hematite are observed at around 530 and 375 nm which are associated with ligand field and ligand-to-metal charge transference, respectively. The thicker film exhibits a fuller shape

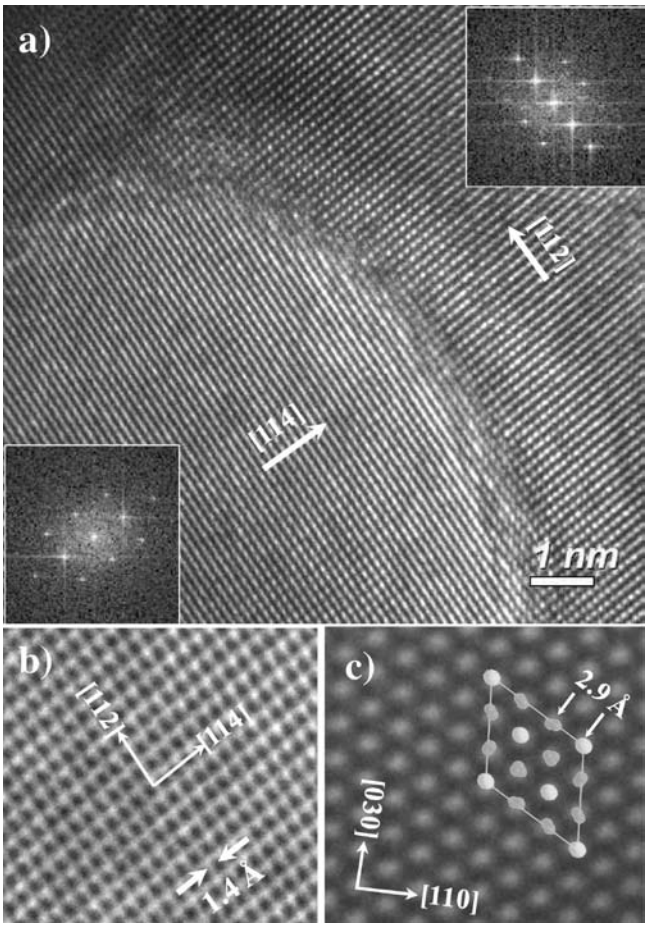

Figure 3. High magnification HRTEM images (a) of a piece of hematite film removed from the substrate (top-view); (b) image simulated considering the FFT analysis pattern performed in two different grains where both grains are oriented along the [110] zone axis; (c) analysis of a columnar grain along the growth direction.

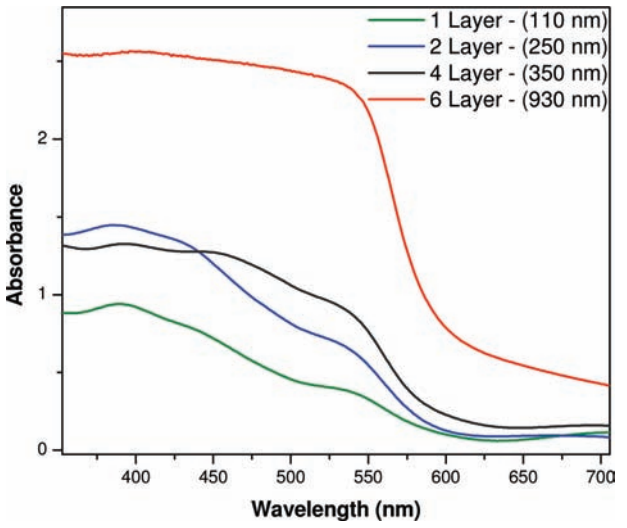

Figure 4. Absorbance spectrum in the region of the UV−vis wavelength of the films with different thickness.

absorption spectrum between the two transitions which is similar to the results reported by Sivula et al.[9] for hematite film processed

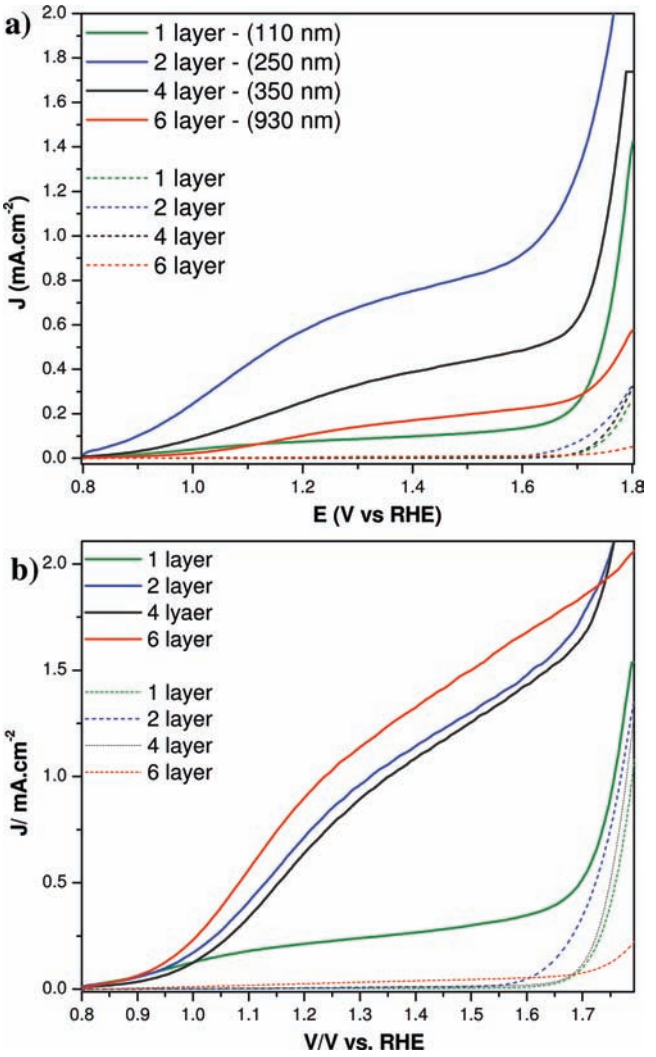

Figure 5. Current−potential curves of the films with different thicknesses: (a) Front-side illumination; (b) back-side illumination. Photocurrent (solid lines) and dark current (dash lines).

by colloidal deposition and sintered at 800 °C. The absorbance spectrum is also characterized by a pre-band gap scattering tail in the range of 600−700 nm which increases in intensity with film thickness. Since this absorption tail is basically promoted by a scattering effect, its contribution to the photocurrent generation must be minimal.

Figure 5 shows the current potential curves of films with different thicknesses under front-side and back-side illumination. As a general trend, the hematite photoanode samples under illumination showed a sharp increase in the photo current around 0.9 V_{RHE} which reached a plateau before the onset of the dark current. The photocurrent performed in the front-side and back-side illumination of the hematite photoanode showed interesting behavior; in the front-side illumination, the two-layer thin film showed the best result with a maximum current of 0.68 mA·cm^{-2} at 1.23 V and thickness of 250 nm. When the film thickness is increased, the current density decreases, and the hematite photoanodes gradually lose efficiency while the continuous thin film thickness increases. Conversely, when the thin-film was illuminated on the back-side, the current density increased gradually with an increase in the film thickness, reaching the

dx.doi.org/10.1021/ja111454f |*J. Am. Chem. Soc.* 2011, 133, 6012–6019

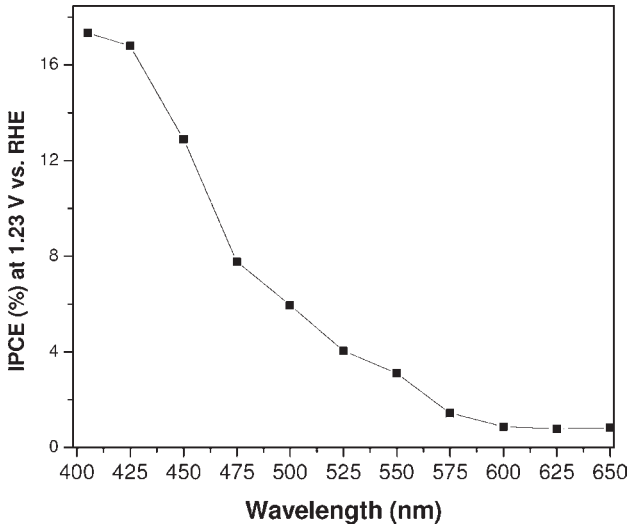

Figure 6. IPCE measurement for the thicker film (930 nm) with back-side illumination at 1.23 V_{RHE}.

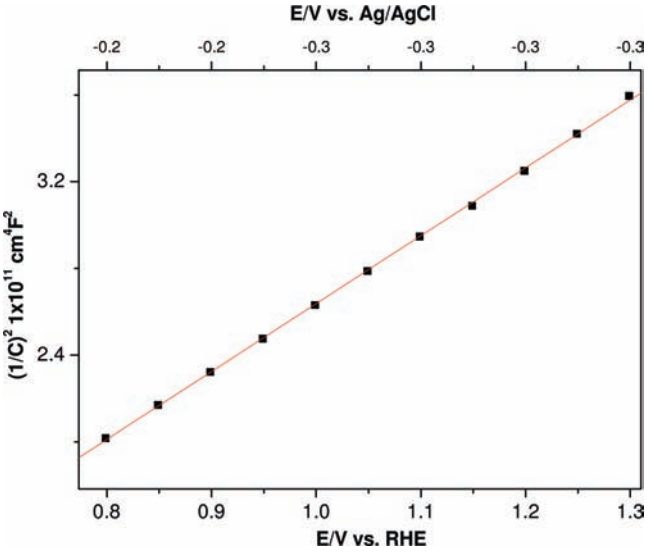

Figure 7. A Mott–Schottky plot for the thicker film (930 nm) recorded in the absence of light (electrochemical impedance analysis performed in a 1 M NaOH electrolyte and a Mott–Schottky analysis performed at 1000 Hz).

highest photocurrent of 1.1 mA·cm^{-2} (at V_{RHE} = 1.23) with a thickness of 930 nm. In both illumination sides, the photoanode showed an overpotential voltage smaller than 0.8 V_{RHE}. In an intermediate thin film thickness, the back-side and front-side illumination have similar photocurrent results. The high photocurrent measured in the back-side illumination must be a consequence of the high connectivity of the elongated pores which allows the penetration of the electrolyte up to the TCO surface. Thus, a high efficiency in the electron collection during the photooxidation must occur. Furthermore, the elongated hematite grain supply is elevated area of solid/electrolyte interface which permits a greater fraction of the photoproduced holes to transfer to the semiconductor–liquid junction and participate in water oxidation. Chronoamperometry measurement, performed at potential of 1.23 V_{RHE}, showed a stable photocurrent (see Figure S5), indicating that unstable species or phases were not present on hematite photoanode.

The incident photon conversion efficiency (IPCE) measurements (see Figure 6) confirm the high efficiency of the mesoporous photoanode under back-side illumination. The thicker film (with 930 nm of thickness) presents IPCE values of 17.5% around 400 nm. To verify the value of the photocurrent at 1.23 V_{RHE}, the IPCE as a function of photon wavelength was examined. Integrating the overlap of IPCE data with the standard solar spectrum (AM 1.5/100 mW·cm^{-2}) gives a calculated value of the photocurrent of 1.3 mA·cm^{-2} (see Figure S4 in the Supporting Information). This value is similar to the value measured by the current–potential curve (1.1 mA·cm^{-2} at 1.23 V_{RHE}) which confirms that the employed light source simulated the AM 1.5 solar emission.

To obtain a better understanding of the charge transport in the hematite photoanodes, a Mott–Schottky analysis was performed to estimate the donor density (N_D) and the flat band potential (V_{fb}). On the basis of the depletion layer model, the capacitance of the semiconductor space charge layer (C_{SC}) is dependent upon the applied potential (V) and can be described by the Mott–Schottky eq 2:

$$\left(\frac{1}{C}\right)^{-2} = \frac{2}{\varepsilon_r \varepsilon_0 e N_D}\left(V - V_{fb} - \frac{k_B T}{e}\right) \qquad (2)$$

where e is the charge of the electron, ε_r is the semiconductor dielectric constant (80 for the α-Fe_2O_3), ε_o is the vacuum permittivity, T is the absolute temperature, and k_B is the Boltzmann constant. Figure 7 shows the Mott–Schottky plot for a thicker film (930 nm) recorded in the absence of light. A good linear fit (with an R^2 of 0.998) was obtained in the bias range from 0.8 to 1.3 V versus RHE. This linear plot suggests that the film obtained by the colloidal deposition process is not formed by complete depletion of the smallest feature size (in our case, the diameter of the textured hematite columnar grain) and/or the columnar grain surface did not present sufficiently high roughness.[20] An N_D of 6.9 × 10^{18} cm^{-3} for the hematite film is calculated from the slope, and a V_{fb} of 0.4 V versus RHE is calculated from the intercept. The N_D value measured in the present study suggests a slightly doped hematite semiconductor material. We can postulate two artifacts that promote this low doping level: (1) unintentional doping caused by the diffusion of Sn^{4+} into the Fe_2O_3 film prepared at high temperatures; and (2) residual carbon impurities or oxygen vacancies in the lattice related to the magnetite oxidation process during photoanode preparation. Considering the unintentional doping and supposing that all of the Sn^{4+} is substitutionally incorporated into the hematite lattice and considering the hematite density (5.28 g/cm^3) and the molar weight of 160 g/mol for the Fe_2O_3, we can estimate a contamination level of ~0.013 atom %, taking into account the N_D value measured in the present study. This value is approximately 2 orders of magnitude smaller than the Sn^{4+} unintentional doping reported by Sivula et al. for a film sintered at 800 °C (1.04% of Sn).[9] Regarding the second artifact, during the heat treatment of the film, the oxidation process of the Fe^{2+} to Fe^{3+} (related to the magnetite oxidation) occurs as well as the oxidation of the organic functional group attached to the magnetite nanocrystal surface (basically the oleyl organic group). These oxidation processes can be the origin of the residual carbon contamination or the oxygen vacancy in the lattice. Recently, Hamann and coauthors[25] reported an N_D value of 7.14 × 10^{18} cm^{-3} for a pure hematite photoanode prepared by

dx.doi.org/10.1021/ja111454f |J. Am. Chem. Soc. 2011, 133, 6012–6019

atomic layer deposition. They speculated that this low doping level must be related to the residual carbon or the oxygen vacancy originating from the ferrocene precursor decomposition. Since Sn was not detected by EDX or XPS analysis, the low dopant level reported in the present work must be related to the presence of residual carbon or an oxygen vacancy.

Regarding the N_D and V_{fb} values, we can estimate the width of the space charge layer (the maximum length of the depletion layer) of ~15 nm for the thicker film (930 nm).[25] The smallest feature size (in our case, the diameter of the textured hematite columnar grain) of the film is ~50 nm, which is larger than the depletion region and confirms the postulation that our film is not fully depleted. On the basis of this analysis, we can estimate a bulk size of ~20 nm (in the core of the columnar grain) for our film. This size is larger than the hole diffusion length in hematite (<5 nm), suggesting a high probability of bulk recombination during the photocurrent generation process. Actually, this analysis indicates that the presence of the space charge layer is fundamental to obtain a photocurrent and that the charge separation is driven by an electric field in the depletion layer. We believe that water oxidation is mainly promoted by the holes located on/or near the depletion layer.

Photoelectrochemical characterization shows that the novel colloidal approach used to process a hematite photoanode produced a high-performance electrode for water photooxidation with an onset potential as low as 0.8 V_{RHE}. This value is comparable to the best results reported in the literature for a hematite photoanode modified with catalytic materials.[10] A high plateau of photocurrent is also observed, even for a film with a grain size in the range of 50 nm. The results reported here (Mott−Schottky analysis) clearly indicate that the colloidal approach used leads to a material with a favorable surface rather than improvement of bulk properties. The lower overpotential and high photocurrent values are attributed to favorable surface properties of the hematite grains obtained by using a high temperature and an oxygen atmosphere during the sintering process. Trevellick et al. addressed two origins for unfavorable surface properties that contribute to the low photocurrent in a hematite photoanode: (1) induced surface reconstruction, at least partially, to a structure that has electrochemical properties very similar to Fe_3O_4 properties. It is well established that the Fe_3O_4 is not a good catalytic material to promote water oxidation;[26,27] and (2) a small intrinsic faradaic rate constant for the oxidation of water on Fe_2O_3 associated with trap levels at or near the surface. It is clear that the extensive grain growth process promoted by the high sintering temperature (higher than the Nell point) and the presence of oxygen must contribute to the stabilization of the surface, avoiding any structure similar to Fe_3O_4. Those treatments must also decrease the surface state recombination as well as recombination in the depletion region. The reason for this modification is not clear and is under investigation; however, we can propose that the high sintering temperature under oxygen flow leads to a passivation of the surface trapping state due to the formation of elongated textured hematite grain with high fraction of (001) surface. In general, it is accept that, in relation to other hematite surface, the (001) surface is relatively inert (in water) to the protonation and deprotonation reactions needed for charge accumulation.[7] This behavior can be favorable to decrease the hematite surface trapping state in water base electrolyte.

As a secondary contribution, the morphology of the photoanode where columnar grains are oriented in a favorable crystallographic orientation for electron collection and the mesoporous structure, which permits the penetration of the electrolyte up to the TCO interface, must also contribute to the high photocurrent. Actually, the greater charge (electron) mobility in a direction perpendicular to [001] should contribute to more efficient charge separation.

CONCLUSION

In conclusion, the results of our study show that magnetite nanocrystals are promising precursors to obtain a hematite photoanode and highlight a different way to explore the photoelectrochemistry of water splitting. We demonstrate that pure hematite thin films reach 1.1 $mA \cdot cm^{-2}$ at 1.23 V_{RHE} with backside illumination. Electrochemical characterization indicates that the method used to process the hematite photoanode leads to a material with a favorable surface rather than an improvement in bulk properties. The surface passivation promoted by the high sintering temperature associated with the textured columnar microstructure resulted in a photoanode with a low overpontential voltage and a high photocurrent.

ASSOCIATED CONTENT

Supporting Information. XRD partterns of magnetite and hematite, SEM images of hematite thickness, STEM and EDX for large hematite structure, XPS spectra, chronoamperometry and integrated solar photocurrent for IPCE data. This material is available free of charge via the Internet at http://pubs.acs.org.

AUTHOR INFORMATION

Corresponding Author
Ricardohg.ufscar@gmail.com; derl@ufscar.power.br

ACKNOWLEDGMENT

The financial support of FAPESP (projects 98/14324-0), FINEP, CNPq (INCT program), and CAPES (all Brazilian agencies) is gratefully acknowledged. We acknowledge Prof. Pedro A. P. Nascente for XPS analysis.

REFERENCES

(1) Dare-Edwards, M. P.; Goodenough, J. B.; Hamnett, A.; Trevellick, P. R. *J. Chem. Soc., Faraday Trans.* **1983**, *79*, 2027–2041.
(2) Itoh, K.; Bockris, J. O. *J. Electrochem. Soc.* **1984**, *131*, 1266.
(3) Bjorkstbn, U.; Moser, J.; Gratzel, M. *Chem. Mater.* **1994**, *6*, 858–863.
(4) Murphy, A. B.; Barnes, P. R. F.; Randeniya, L. K.; Plumb, I. C.; Grey, I. E.; Horne, M. D.; Glasscock, J. A. *Int. J. Hydrogen Energy* **2006**, *31*, 1999–2017.
(5) Kay, A.; Cesar, I.; Gratzel, M. *J. Am. Chem. Soc.* **2006**, *128*, 15714.
(6) Moser, J.; Gratzel, M. *Helv. Chim. Acta* **1982**, *65*, 1436–1444.
(7) Yanina, S. V.; Rosso, K. M. *Science* **2008**, *320*, 218–222.
(8) Ahrned, S. M.; Leduc, J.; Haller, S. F. *J. Phys. Chem.* **1988**, *92*, 6655–6660.
(9) Sivula, K.; Zboril, R.; Formal, F.; Le; Robert, R.; Weidenkaff, A.; Tucek, J.; Frydrych, J.; Gratzel, M. *J. Am. Chem. Soc.* **2010**, *132*, 7436–7444.
(10) Tilley, S. D.; Cornuz, M.; Sivula, K.; Gratzel, M. *Angew. Chem., Int. Ed.* **2010**, *49*, 1–5.
(11) Hu, Y.-S.; Kleiman-Shwarsctein, A.; Forman, A. J.; Hazen, D.; Park, J.-N; McFarland, E. W. *Chem. Mater.* **2008**, *20*, 3803–3805.

(12) Sartoretti, C. J.; Alexander, B. D.; Solarska, R.; Rutkowska, I. A.; Augustynski, J. *J. Phys. Chem. B* **2005**, *109*, 13685–1369.
(13) Zhong, D. K.; Sun, J.; Inumaru, H.; Gamelin, D. R. *J. Am. Chem. Soc.* **2009**, *131*, 6086–6087.
(14) Kanan, M. W.; Nocera, D. G. *Science* **2008**, *321*, 1072–1075.
(15) Steinmiller, E. M. P.; Choi, K.-S. *Proc. Natl. Acad. Sci. U.S.A.* **2009**, *106* (49), 20633–20636.
(16) Shiroishi, H.; Nukaga, M.; Yamashita, S.; Kaneko, M. *Chem. Lett.* **2002**, *31*, 488–489.
(17) Gonçalves, R. H; Cardoso, C. A.; Leite, E. R. *J. Mater. Chem.* **2010**, *20*, 1167–1172.
(18) Schuler, T.; Krajewski, T.; Grobelsek, I.; Aegerter, M. A *Thin Solid Films* **2006**, *50*, 67–71.
(19) Smith, R. W.; Fuller, M. *Science* **1967**, *156*, 1130–1134.
(20) Cesar, I.; Sivula, K.; Kay, A.; Zboril, R.; Gratzel, M. *J. Phys. Chem. C* **2009**, *113*, 772–782.
(21) Souza, F. L.; Lopes, K. P.; Longo, E.; Leite, E. R. *Phys. Chem. Chem. Phys.* **2009**, *11*, 1215–1219.
(22) Dalmashio, C. J.; Ribeiro, C.; Leite, E. R. *Nanoscale* **2010**, *2*, 2336.
(23) Marusak, L. A.; Messier, R.; White, W. B. *J. Phys. Chem. Solids* **1980**, *41*, 981.
(24) Gilbert, B.; Frandsen, C.; Maxey, E. P.; Sherman, D. M. *Phys. Rev. B* **2009**, *79* (3), 035108.
(25) Klahr, B. M.; Martison, A. B. F.; Hamann, T. W. *Langmuir* **2011**, *27* (1), 461.
(26) Trasatti, S. *J. Electroanal. Chem.* **1980**, *111*, 125.
(27) Walter, M. G.; Warren, E. L.; McKone, J. R.; Boettcher, S. W.; Mi, Q.; Santori, E. A.; Lewis, N. S. *Chem. Rev.* **2010**, *110*, 6446–6473.